Aerodynamic characteristics and excitation mechanisms of the galloping of an elliptical cylinder in the critical Reynolds number range

Wenyong Ma[a,b], J.H.G. Macdonald[c], Qingkuan Liu[a,b]

[a]Wind Engineering Research Center, Shijiazhuang Tiedao University, Hebei 050043, China

[b]The Key Laboratory for Health Monitoring and Control of Large Structures, Hebei province, 050043, China

[c]Department of Civil Engineering, University of Bristol, BS8 ITR, UK

Abstract: The generation mechanisms of dry cable instabilities in the critical Reynolds number range are still unclear because of their complicated aerodynamic forces and a shortage of studies on the coupling process. Large amplitude vibrations of an elliptical cylinder in the critical Reynolds number range are reproduced in a wind tunnel, and displacements and wind pressure on the cylinder are recorded synchronously to illustrate the interactions between the cylinder motion and the aerodynamic forces in this study. Strong interactions are observed only when the flow starts reattaching at the rear of the cylinder in the early critical Reynolds number range, wherein the reattachment stops the Kármán vortex shedding and forms a separation bubble. Once the reattachment points move forward, large amplitude vibrations are not observed. The vibration is strongly related to the contribution of the pressure in the region of the separation bubble. The organization of aerodynamic forces along the length is also needed to cause the vibrations. The aerodynamic forces are not uniformly distributed along the cylinder in the critical Reynolds number range and they can either input or absorb energy during the vibrations.

Keywords: Wind tunnel test; Elliptical cylinder; Critical Reynolds number;Dry galloping; Coupling effect

1. Introduction

Large amplitude vibrations of dry circular cylinders in the critical Reynolds number range have been reproduced in wind tunnel experiments (Benidir et al., 2015; Jakobsen et al., 2012; Matsumoto et al., 2010; Matteoni and Georgakis, 2015; Nikitas and Macdonald, 2015; Nikitas et al., 2012). The mechanism of these vibrations, which are called dry galloping, is not yet clear due to the complexity of aerodynamic forces at critical Reynolds numbers. As it has been observed only on dry inclined cables in wind tunnels, the phenomenon could be attributed to a lack of circularity (Benidir et al., 2015; Flamand and Boujard, 2009; Matteoni and Georgakis, 2012, 2015), axial flow (Matsumoto et al., 2010) or the critical Reynolds number (Nikitas and Macdonald, 2015). The common understanding is that the critical Reynolds number definitely plays an important role for exciting the dry galloping.

In the critical Reynolds number range, flow around a circular cylinder exhibits a single bubble regime, whereby the transition occurs on one side of the cylinder and flow reattaches to cylinder on that side; and a two bubble regime, whereby the flow reattaches symmetrically on both sides (Benidir et al., 2015; Zdravkovich, 1997). The single bubble can produce a reattachment-type pressure distribution at high wind velocities, which may excite large vibrations; Meanwhile, Kármán vortex shedding is suppressed by the interruption of communication between the separation flows on both sides (Matsumoto et al., 2010). Studies have already shown that the flow in the critical Reynolds number range is sensitive to external disturbances or stimulations (Hoxey et al., 1998; Schewe, 1986; Zdravkovich, 1997). This sensitivity may be caused by the released separated flow from the control of the Kármán vortex (Matsumoto et al., 2010) and may allow an easier interaction between the fluid and the moving cylinder in the critical Reynolds number range. Unfortunately, it is difficult to distinguish the effects of reattachments induced by the occurrences of transitions in the boundary layer and those of the suppression of the Kármán vortex shedding since they occur together. Matsumoto et al. claimed the interaction could induce unsteady galloping whose response characteristics cannot be explained by quasi-steady theory, and the fluid-cylinder interaction of galloping in the critical Reynolds number range is worthy of further study. Nikitas and Macdonald have discussed the aerodynamic force characteristics of dry galloping, and their results show a periodic change in wind pressure on one side of the cylinder where the separation bubble is not fully formed, while the wind pressure hardly changed during the vibrations on the side with a stable separation bubble (Nikitas and Macdonald, 2015). This illustrates that the reattachment on the side with the separation

bubble contributes little to the large vibrations and implies that the reattachment may not be a necessary condition for the vibrations, which makes the situation even more complex. Their results also show that the aerodynamic forces on different pressure rings spread along the cylinder have distinctly different contributions to the excitations. Noting the sensitivity of the aerodynamic forces in the critical Reynolds number range; and that, in reality, any tested model and approaching flow are not perfectly uniform, the aerodynamic force distribution along the cylinder axis is also worth considering. Thus, the analysis of the variations of aerodynamic forces on a vibrating cylinder in the critical Reynolds number range could be very helpful for understanding the mechanism of dry galloping and identifying the effects of reattachment and the suppression of vortex shedding.

Reattachment and separation bubbles also occur on cylinders with other curved cross-sections, such as elliptical and semi-elliptical sections, at Reynolds numbers, which is of concern to civil engineers (Alonso et al., 2010; Ma et al., 2015). These shapes share similar features in the critical Reynolds number range to a circular cylinder, but they have a clear definition of the angle of attack, which could be important when considering the lack of circularity. For a circular cylinder, the single separation bubble regime is exhibited only in a narrow Reynolds number range before regular vortex shedding reappears when separation bubbles form on both sides. For an unsymmetrical shape, the wide Reynolds number range in which flow reattaches to only one side of the cylinder can provide a better chance of identifying the effects of reattachment and the suppression of vortex shedding.

In this paper, a cylinder with an elliptical cross-section and a major to minor axis ratio of 1.5 is tested in a wind tunnel. The wind pressure on the cylinder is measured in both static and dynamic tests. The displacements of and wind pressures on the cylinder are recorded synchronously during the dynamic tests to obtain the variations in the aerodynamic forces and vibrations. By analysing the responses of and aerodynamic forces on the cylinder for large amplitude galloping in the critical Reynolds number range, the present work aims to reveal the process of the fluid-cylinder interactions and effects of the distribution of the spanwise aerodynamic forces on the vibrations.

2. Experimental setup and procedure

A series of static and dynamic tests were carried out using the same elliptical cylinder in a wind tunnel STDU-1 at Shijiazhuang Tiedao University, in the large test section which is 4.38 m wide, 3 m high and 24 m long. The longitudinal turbulence intensity was approximately 0.5% and the wind velocity was within ±0.5% over the cross-section at a wind speed of 20 m/s. The elliptical cylinder model, which was made of polyethylene pipe, had a length L=2.9 m, minor axis D=180 mm and major axis 1.5 D and was mounted normal to the flow. A steel pipe with a diameter of 30 mm was in the center of the model to provide the stiffness of the cylinder. The maximum blockage ratio was 6% in this study.

The surface wind pressures were measured in all the tests by 320 pressure taps arranged on four discrete cross-sections, termed Ring A, B, C and D, and four lines, termed L1, L2, L3 and L4 (see Fig. 1). Each ring had 50 pressure taps that were uniformly distributed around the circumference. Rings A and D were placed 85 cm from the ends, Ring C was in the middle of the cylinder, Ring B was 20 cm away from Ring C and Ring A was a further 40 cm away. 30 pressure taps were uniformly arranged along the cylinder on each line between points 8.7 cm away from each end. The wind pressures were recorded with pressure sensors (ESP-64Hd, Measurement Specialties (formerly PSI), Hampton, VA, USA) and a data acquisition system (DTC Initium, Measurement Specialties). The pressure tubes were 800 mm in length, and their effects on the pressure distortion were corrected by using the theoretical frequency-response function of each tube.

To reduce the adverse effects of the free end within the wind tunnel, a 2.28 m long end plate with a 300 mm diameter hole in the centre and a 2 m long end cover with the shape of a NACA2420 aerofoil was used on each end. The ends of the cylinder and the support system, including springs and end bars were enclosed by the end plates and covers in this arrangement. Each end plate is approximate 810 mm away from wind tunnel wall (Fig. 1 (c)). The hole in the center of the end plate provided a space for vibration, and the NACA2420 end cover made the flow less likely to

separate, reducing its influence on the downstream flow.

In the dynamic tests, the cylinder was supported by four inclined springs at each end (Fig. 1 (d)). These springs allow three-degree-of-freedom (3DOF) motion. The dynamic responses were measured synchronously with wind pressure using five laser displacement sensors (Panasonic HL-G112-A-C5). At each end, two displacement sensors were mounted to measure the vertical displacements of both ends of the end bar. Another sensor measured the horizontal displacement at one end. For each record, the data were recorded for more than 80 s with a sampling frequency of 500 Hz.

The static tests were carried out first. The end bar was connected to the wind tunnel walls with four steel bars to keep the cylinder stationary during the tests. The wind speeds were from 5 m/s to 20 m/s, corresponding to Reynolds numbers from approximately 0.61×10^5-2.45×10^5 (based on the minor axis D). The angles of attack α spanned from wind parallel to the major axis 0° to parallel to the minor axis 90° at 10° spacing in general range and 2° spacing for 20°-30°.

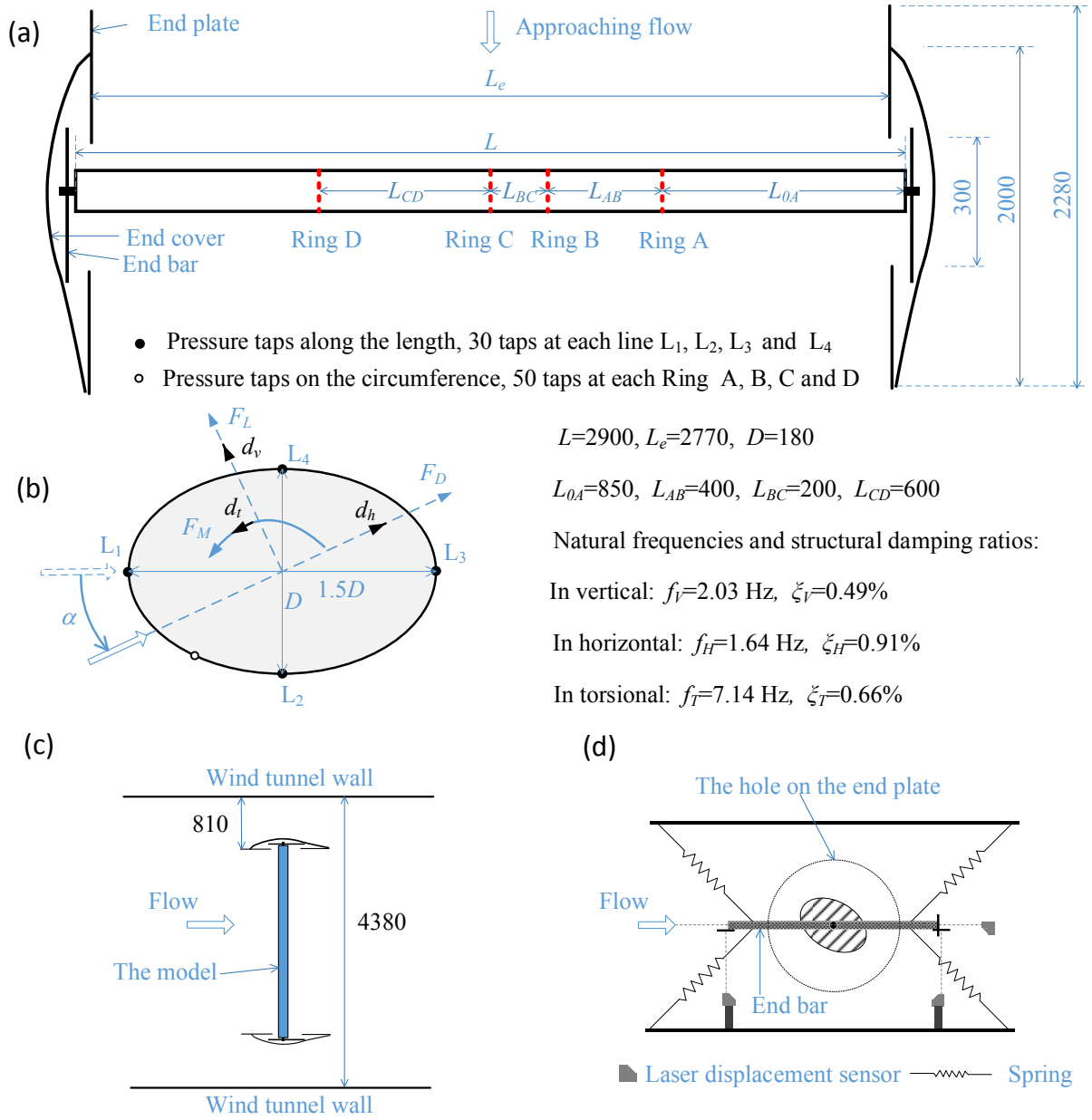

Fig. 1. Schematics of the wind tunnel arrangement and the model with the main parameters indicated: (a) model and end conditions, (b) cross-section and pressure tap arrangement, (c) model in wind tunnel, (d) support system at the end.

For the dynamic study, free vibration tests were carried out to obtain the decay of the displacements vertically d_v, horizontally d_h and torsionally d_t; before performing dynamic tests, wherein the four steel bars were replaced by spring supports. The natural frequencies and damping ratios were identified using the Fast-Fourier-Transform and the logarithmic decrement of the displacement. The identified natural frequencies and damping ratios were f_v=2.03 Hz and ξ_v=0.49% vertically, f_h=1.64 Hz and ξ_h=0.91% horizontally and f_t=7.14 Hz and ξ_t=0.66% torsionally.

In the dynamic tests, an initial angle of attack α_0 was set and the displacements and wind pressures with no wind were recorded. When the wind speed was increased to a certain value, the wind speed and cylinder motion were allowed to settle for approximately 2 minutes before and after recording the data. The wind speed was measured using a Pitot tube one metre ahead of the cylinder. At each wind speed, the recorded displacements were used to identify both the dynamic responses and the cylinder's mean position, including the mean angle of attack α. Unlike in the static tests, the mean angle of attack in the dynamic tests depended on α_0, the stiffness of the supporting system and the wind speed. The initial angles of attack α_0 were chosen, considering the aerodynamic forces obtained from the static tests and the stiffness of the supporting system from the free vibration tests. Values of α_0 =23.20°, 24.50°, 25.50°, 26.00° and 28.00° were chosen, and large amplitude vibrations were subsequently observed for α_0 =25.50° and 26.00°. Wind speeds from 2.4 m/s to 18 m/s were used, with varying intervals for different α_0.

3. Dry galloping occurrence and its characteristics

The large vibrations observed in this study are termed 'dry galloping' because vibration in the critical Reynolds number range is complicated and similar vibrations of circular cylinders have been named 'dry galloping'. Many large vibrations were observed in the dynamic tests and had been reported in another paper (Ma et al., 2017), but the interactions of the aerodynamic forces and vibration need further detailed analysis. The large vibrations were observed in the ranges Re=1.5×10^5-1.8×10^5 and α=26.5°-27.5° (note that α_0 is the angle of attack without wind and α is the mean angle of attack with the wind). This range includes steady amplitude galloping and unsteady, increasing and decreasing amplitude vibrations as well. Since the support system in this study allows motion with three degrees of freedom, the mean angle of attack changes with increasing wind speeds. Galloping occurs at a specific combination of Reynolds numbers and mean angles of attack and diminishes when either the Reynolds number or the mean angle of attack is out of the range, such that the galloping is clearly a joint effect of the Reynolds number and angle of attack.

As an example of steady galloping, part of a record of the displacement observed at α=26.98° and Re=1.75×10^5 is shown in Fig. 2 (a), and their power spectral densities (PSDs) are shown in Fig. 2 (b). The vertical displacement exhibits quite steady periodic vibrations, while there are many small amplitude jumps in the horizontal direction. The maximum variations of the horizontal displacements from the mean are approximately 5% of D or 13% of the mean vertical amplitude (the amplitude of each cycle is defined as half the peak to peak displacement). The torsional amplitude is less than 0.01 radians, and the measured fluctuating relative angle of attack induced by the rotation is 11.9% of the value induced by the mean amplitude of the vertical velocity. The PSDs of the vertical displacement shows a significant peak at the vertical natural frequency (2.03 Hz) while the horizontal and torsional displacements do not show significant peaks in their natural frequencies (1.64 Hz and 7.14 Hz, respectively). Based on the results that show that the horizontal and torsional responses are much smaller than the vertical response and are not dominated by resonant vibrations, the cylinder vibrations can be treated as vertically dominated, i.e., across-wind dry galloping. Furthermore, the substantial differences in the natural frequencies in the three degrees of freedom are explained to weaken the effect of any coupling.

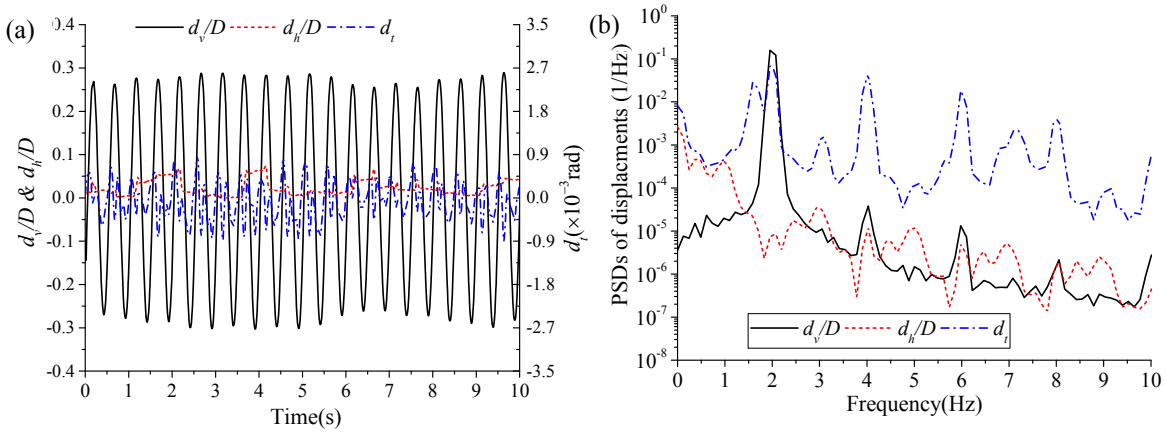

Fig. 2. The occurrence of galloping: (a) Time histories of the displacements and (b) power spectral densities of displacements.

Taking α_0 =25.5° as an example, Fig. 3 shows the variations of the mean normalized vertical amplitudes and mean lift coefficients on the four rings with Reynolds numbers and reduced velocities (U/f_vD). In this case, large amplitude vibrations occur at α=26.8°-27.0° and Re=1.6×10^5-1.8×10^5, corresponding to the reduced velocities from 35.6 to 40.1 which seems high enough to satisfy the quasi-steady assumption, according to Fung's (Fung, 1955) and Blevin's (R.D.Blevins, 2001) recommendations. The significant differences in the mean lift coefficients on the four rings shown in Fig. 3 indicate that the mean aerodynamic force distribution along the length of the cylinder is far from uniform during the vibrations within the critical Reynolds number range. The increase of the lift coefficient, which represents flow reattachment on one side of the cylinder, occurs at around Re=1.35×10^5 on Rings B and C and at Re=1.95×10^5 on Ring D, illustrating a clear difference in the aerodynamic forces on the four rings once the reattachment occurs. In this case, the aerodynamic forces on Rings B and C are in the critical regime when the cylinder experiences large vibrations. Although the flows around Rings B and C show similar features with the occurrence of reattachment, they differ from each other in the strengths and variations of C_L with changes in the Reynolds number. The lift coefficients on both rings exhibit a clear change when the vibration amplitude drops at Re=1.75×10^5-1.79×10^5. There are no noticeable changes in the lift coefficients on Rings A and D in the Reynolds number range for large vibrations. The flows at these two rings in this Reynolds number range are subcritical, with no reattachments, although Ring D exhibits a critical flow for Re>1.95×10^5 without any significant vibrations. Identifying a clear link between the vibrations and the mean aerodynamic forces is difficult because there are at least three different types of behaviours of the mean lift coefficient for the same vibration process. This will be discussed in Section 4. Based on Fig. 3, the aerodynamic force distribution along the length of the cylinder and the dynamic interaction between the forces and the vibrations are worth further consideration, which will be discussed in Section 5.

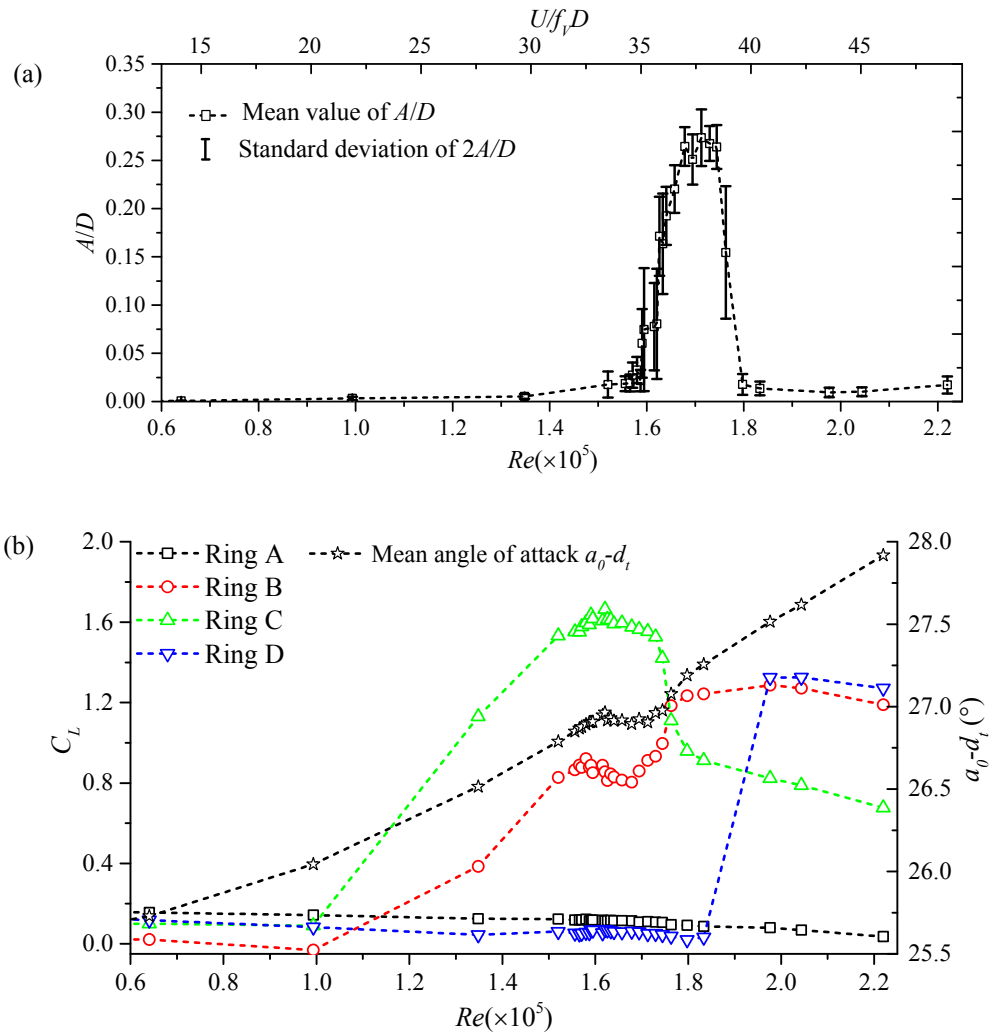

Fig. 3. (a) Mean and standard deviations of normalized amplitude, (b) mean angle of attack and mean lift coefficients in term of Reynolds number at α_0=25.5°.

4. Interaction between vibrations and the aerodynamics

4.1 Assessment of the quasi-steady assumption

Although Matsumoto (Matsumoto et al., 2010) and Matteoni (Matteoni and Georgakis, 2015) implied that the quasi-steady assumption might not explain the dry cable instability phenomenon at critical Reynolds numbers, a clear relationship of lift coefficients to the relative angles of attack has not been reported because in these previous studies the angle of attack is not well defined. In this study on elliptical cylinders with well-defined reference orientations, the angle of attack is formed by considering the initial angle of attack α_0, torsional motion d_t(t), vertical velocity v_v(t) (derivative of d_v(t) with respect to time), horizontal velocity v_h(t) (derivative of d_h(t) with respect to time), and wind speed U.

$$\alpha_r(t) = \alpha_0 - d_t(t) + \arctan\left(\frac{v_v(t)}{U - v_h(t)}\right) \quad (1)$$

In the present study, the relative angle of attack is mainly induced by the vertical velocity. An example in Fig. 2 (a) indicates that maximal d_t(t) is approximate 11.9% of mean angle of attack induced by v_v(t). Due to the wide range of

frequency components in the aerodynamic forces for flow in the critical Reynolds number range, it is hard to recognize a pattern of the variations of the lift coefficients with the relative angles of attack. See the grey dashed line in Fig. 4 (a) for f<40 Hz. Fig. 4 (a) also shows the variation of a bandpass filtered lift coefficient (in solid line) in a small range frequency 1.9Hz < f <2.1Hz, around the dominating frequency of the vibration 2.01 Hz in this case. Another method proposed by Nikitas and Macdonald (Nikitas and Macdonald, 2015) is to use phase averaging. In this study, the phase averaged results are based on the vertical displacement responses, obtained by dividing each record into around 160 individual cycles. The responses and aerodynamic forces are averaged in phase to derive an equivalent single average cycle. Taking the steady amplitude vibrations at α_0 =25.5°, α=26.98°and Re=1.75×10^5 as an example, the variations of the phase averaged lift coefficients with the phase averaged relative angle of attack for the four tested rings are shown in Fig. 4 (b) using open symbols and dotted lines. The open upward triangle represents the phase averaged lift coefficient for Ring C based on the original data shown in Fig. 4 (a). The lift coefficients obtained from the static tests are also shown in Fig. 4 (b) using solid symbols and dashed line. Unfortunately, the static results are for slightly different conditions, with Re=1.72×10^5. The phase averaged dynamic lift coefficients on the four rings show the significant differences in the static lift coefficients in Fig. 3. Two obvious traits of the dynamic lift coefficients reveal that they do not satisfy the quasi-steady assumption. First, the dynamic lift coefficients, especially those for Rings B and C, do not follow the static lift coefficients, with a declination with increasing angles of attack, which could result in negative aerodynamic damping based on Den Hartog's criterion. Second, the curves of the lift coefficient for Rings B and C against the relative angle of attack show that they are not simply a function of the angle of attack, meaning that the aerodynamic forces cannot be treated as being only velocity-dependent, which is a basic feature of the quasi-steady assumption. The mean dynamic and static lift coefficients agree quite well for Rings A, B and D. The difference of Ring C may reflect the sensitivity of the occurrence of the reattachment to small differences in the Reynolds number (dynamic test at Re=1.75×10^5 and static test at Re=1.72×10^5) and to the vibrations.

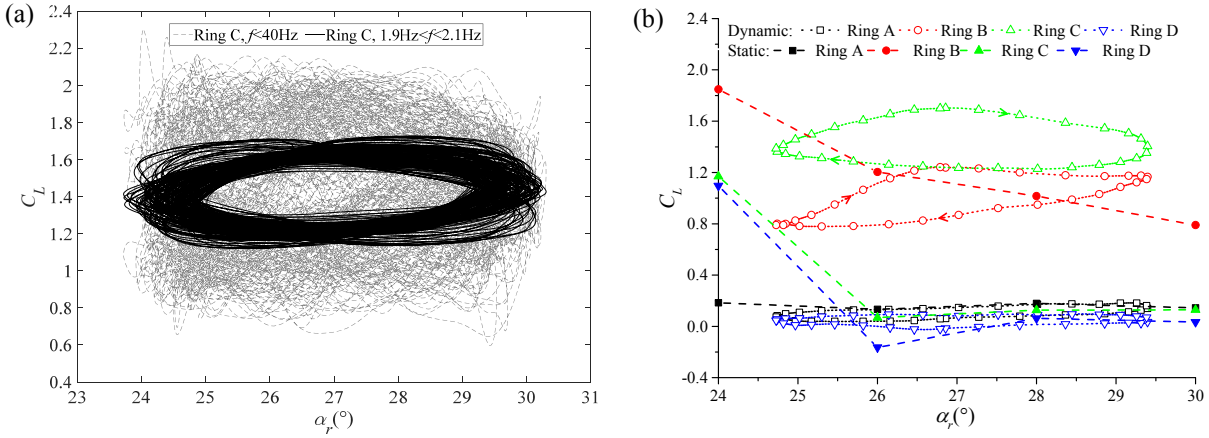

Fig. 4. Variation of lift coefficients with the relative angle of attack at (a) dynamic tests, Ring C with frequency components f<40Hz and 1.9Hz<f<2.1Hz, and (b) static and dynamic tests, four rings with phase averaging in dynamic tests.

4.2 Aerodynamic characteristics

The aerodynamic forces significantly change in the critical Reynolds number range because of the formation of separation bubble. According to flow states around a circular cylinder(Zdravkovich, 1997), the separation bubble, which is between the first separation point and reattachment point, can be identified by the sudden drop in pressure coefficient with increasing Reynolds number. It also can be estimated by the sudden change in lift coefficient (Fig. 3) because the drop in pressure coefficient commonly occurs on the flank of the cylinder, which contributes a lot to the lift coefficient. The reattachment point is ahead of the final separation point when flow reattachs on the cylinder. Fig. 5

shows estimation of the final separation bubble for three types of wind pressure distribution observed in static tests. In the present study, the final separation points are approximately estimated through the mean value and standard deviation of pressure coefficient distribution by four principles. Firstly, the final separation point is at inflection of the curves of pressure coefficient against angular angle θ, which starts at the stagnation point (solid circle in Fig. 5) and increase clockwise. Secondly, it is behind minimal wind pressure point. Thirdly, the Pressure distribution becomes uniform after the final separation point. Finally, the standard deviation of pressure coefficient $C_{P\sigma}$ is relatively large due to the strong fluctuation at the point. Based on these principles, the final separation points are approximately $\theta \approx 50°$, 110° and 65° in Fig. 5 (a), (b) and (c), respectively. The flow reattaches between minimal pressure to the final separation point. The reattachment range in Fig. 5 (b) is wider and more leeward than it in Fig. 5 (c). Unfortunately, it is hard to identify the reattachment point through wind pressure distribution because the reattachment is an unsteady process and related to the random burst of separation bubble.

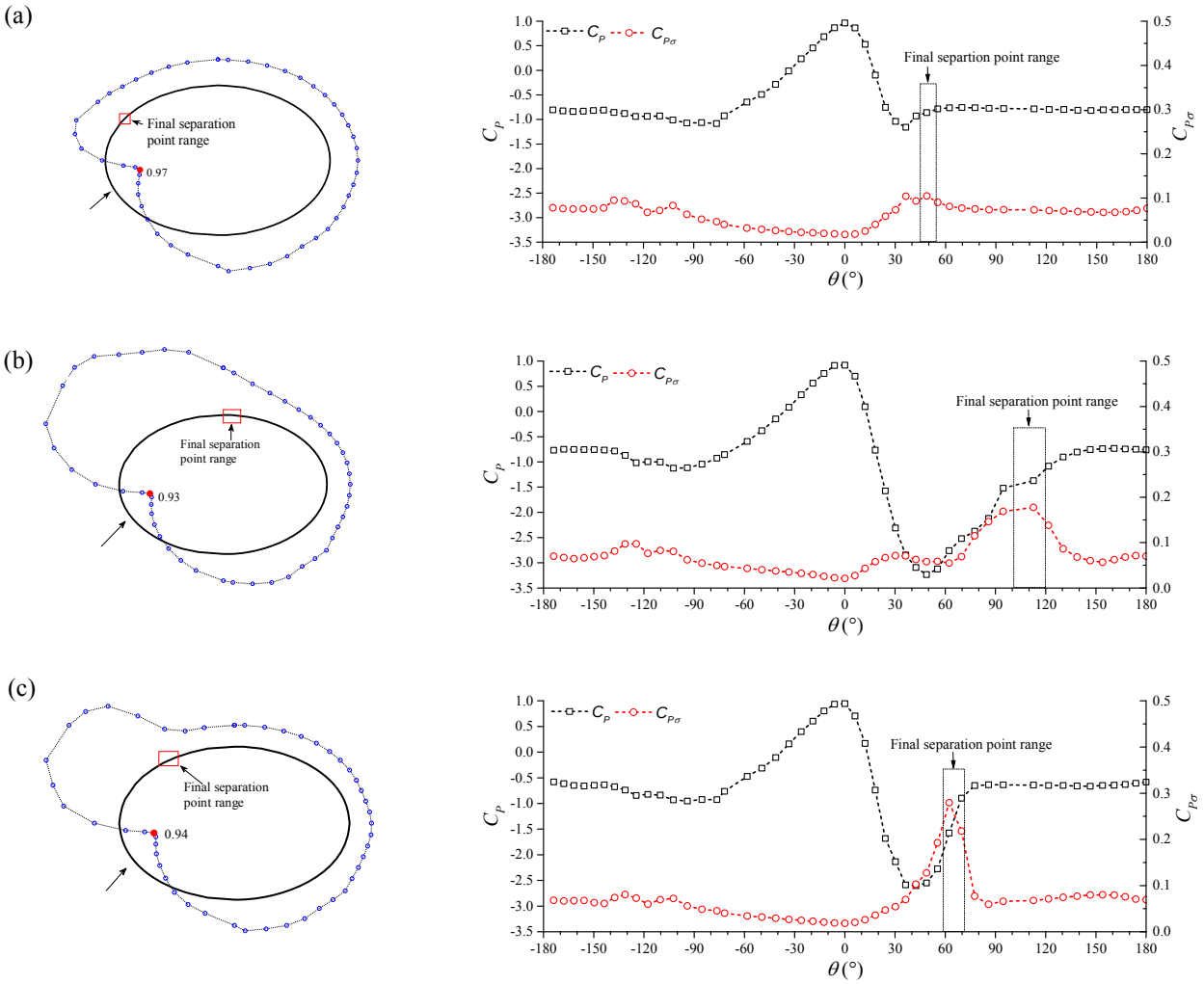

Fig. 5. Estimation of the final separation point range through wind pressure distribution at (a) Re=1.95×10^5, α=26°, (b) Re=1.72×10^5, α=26°, (c) Re=2.22×10^5, α=26°

By showing the distributions and PSDs of the lift coefficients on the four rings, Fig. 6 aims to further illustrate the characteristics of the aerodynamic forces when the cylinder experiences large vibrations as shown in the normalized displacement time history of Fig. 6 (a) (with α=26.98°, Re=1.75×10^5). The solid line, dashed line, dot symbol and shadow between the dotted lines are edge of the cross-section, the mean pressure coefficients (C_P), the maximum positive mean pressure coefficients representing the average stagnation point and a range of the mean plus and minus of standard deviations of the pressure coefficients ($C_P \pm C_{P\sigma}$), respectively.

The amplitudes in Fig. 6 (a) show little variation with time over 80 s. The mean pressure coefficient distributions on the rings reconfirm the reattachments on Rings B and C, as concluded from Fig. 3. The wind pressure coefficients show large fluctuations on Rings B and C in the separation bubble region between the points of first separation and reattachment on the upper side of the cylinder. The PSDs of the lift coefficients on the four rings reveal that the interactions of the cylinder motion and the aerodynamic forces are much stronger on Rings B and C than on Rings A and D since there is a much greater forcing at the vertical vibration frequency, 2.01Hz. As expected, vortex shedding does not appear when the flow reattaches on Rings B and C, since the communication between the flow separated from both sides is interrupted. However, vortex shedding, which was observed at lower Reynolds numbers, has disappeared on Rings A and D, where there is no clear sign of reattachment. A possible reason for this is that the reattachment has a wide influence on the flow of the wake because of mixing turbulence after the transition, which induces a three-dimensional flow state around the cylinder. Another possibility is that the vortex shedding is interrupted once the laminar to turbulent flow transition occurs in the vortex formation area in the wake, which is very close to the rear of the cylinder, rather than in the boundary layer of the cylinder. This state has been called precritical (Zdravkovich, 1997). By comparing Fig. 3 and Fig. 6, the large vibrations are shown to be strongly related to aerodynamic forces which show characteristics of reattachment in the critical Reynolds number range. The main contribution to the dynamic forcing is the wind pressure fluctuations in the region of the separation bubble, which are related to the interactions with the motion.

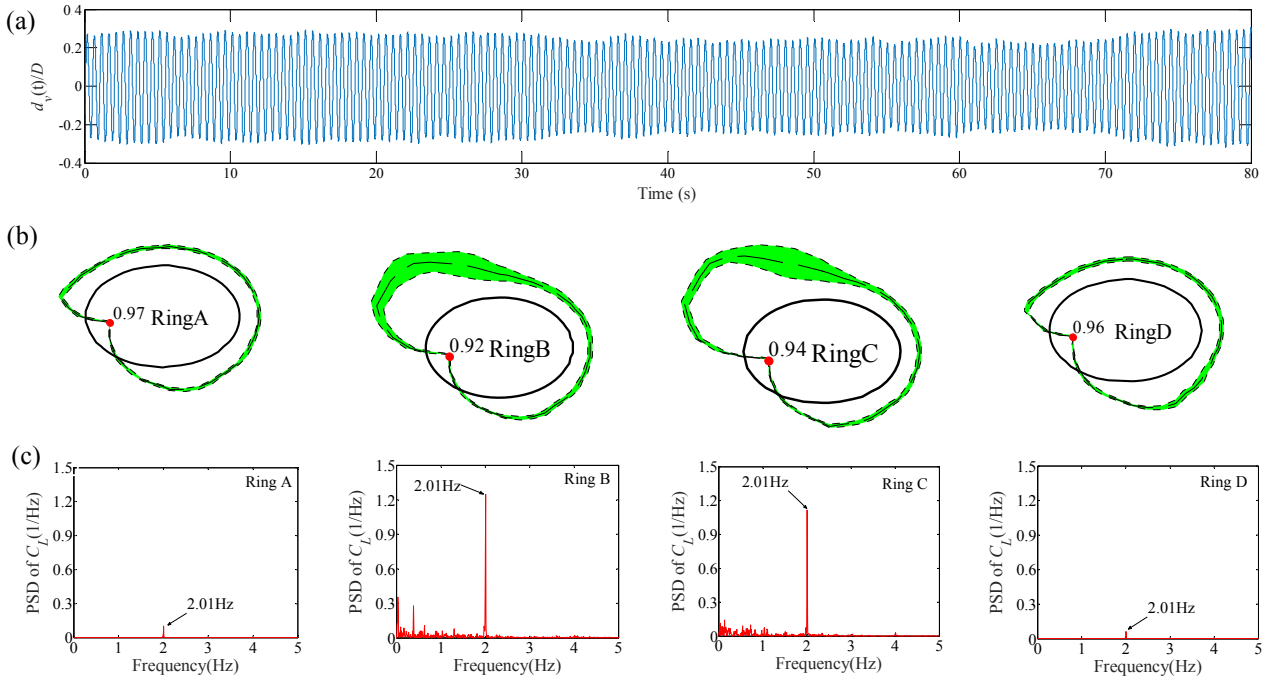

Fig. 6. Displacement, wind pressure coefficient distribution and power spectra of the lift of a steady amplitude vibration at α=26.98° and Re=1.75×10^5; (a) vertical normalized displacement, (b) mean and standard deviation pressure coefficient distribution on the four rings and (c) power spectra of lift coefficients on the four rings.

4.3 Interaction process

The effects of the aerodynamic forces on the vibrations can be identified by calculating the energy input. The cumulative energy input up to time t_e is defined as the sum of the products of the instantaneous lift coefficients (mean values subtracted) times the vertical velocities over the time from 0 to t_e. The instantaneous displacement and the lift coefficients on Rings A and C as well as their cumulative energy inputs are shown in Fig. 7. The lift coefficients are also filtered through a narrow range of frequencies from 1.9 Hz to 2.1 Hz to illustrate the variations of the lift

coefficients around the frequency of vibration, 2.01 Hz. The cumulative energy input of the lift on Ring A exhibits a linear declination with time. This indicates that the lift on Ring A continuously takes energy out of the system during the vibrations. Hence some aerodynamic forces, such as those on Ring A, tend to reduce vibrations rather than excite them. Unlike simply extracting energy , as occurs on Ring A, the lift on Ring C follows a complex process in its energy exchange during the vibrations. The cumulative power input of the lift on Ring C is mostly above zero, which indicates that the lift generally inputs energy. However, the occasional declination with time also indicates that the lift on Ring C occasionally takes energy out. The instantaneous lift coefficient on Ring C varies with time in both amplitude and phase delay with respect to displacement. The amplitude of the lift affects the rate of energy exchange, but the phase delay determines whether the force inputs or absorbs energy as well as affecting the rate. It should be emphasized that the aerodynamic forces on Rings A and C describe only two patterns existing during the vibrations. There may be other patterns as well. Even though it seems that the variations of the cumulative energy input of lift on Ring C agree well with the variations in amplitude shown in Fig. 7, the vibration depends on the total aerodynamic forces on the cylinder, which can not be estimated using only the results of the four individual rings.

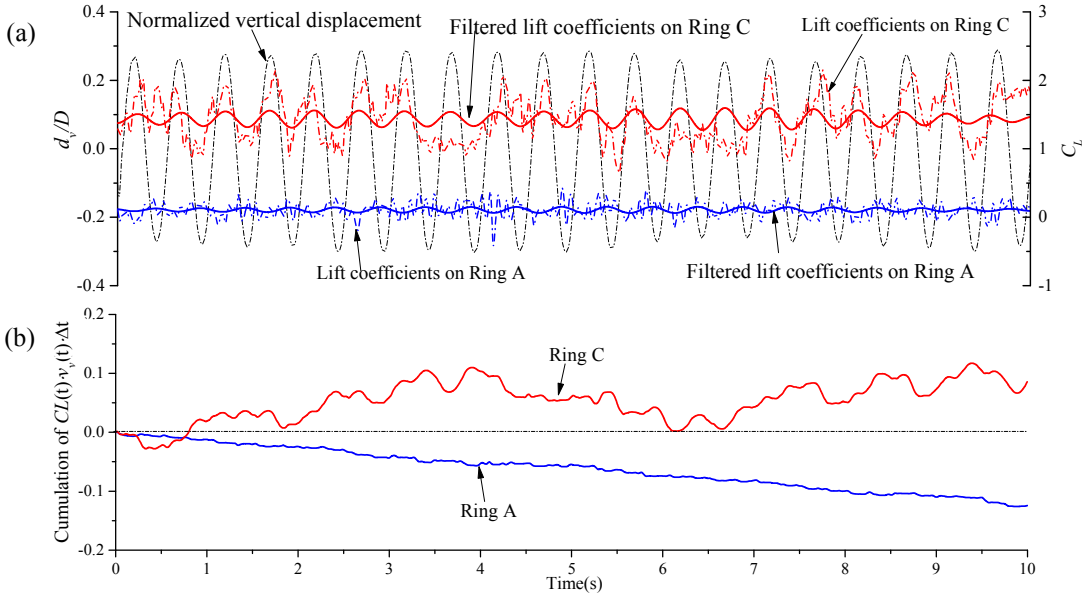

Fig. 7. (a) Instantaneous vertical displacement and lift coefficients, and (b) cumulative energy input on Ring A and C over 10 s at α=26.98° and Re=1.75×10^5.

Nikitas and Macdonald used the phase averaged pressures to illustrate the variations of their distributions for a circular cylinder in motion (Nikitas and Macdonald, 2015). This method is able to show the interaction process as an averaged cycle without the distraction of noise components, although it loses the details of the variations of each cycle. The phase averaged vertical displacement d_v, vertical velocity v_v, lift coefficients C_L, power input $C_L(\varphi)\times v_v(\varphi)$, and pressure coefficient distributions averaged over 160 cycles, are shown in Fig. 8. In Fig. 8 (d), the solid line, dashed line, open circles and solid circles represent the shape of the cross-section, the mean pressure coefficient distribution, the phase averaged pressure coefficients and the maximum mean pressure coefficients, respectively.

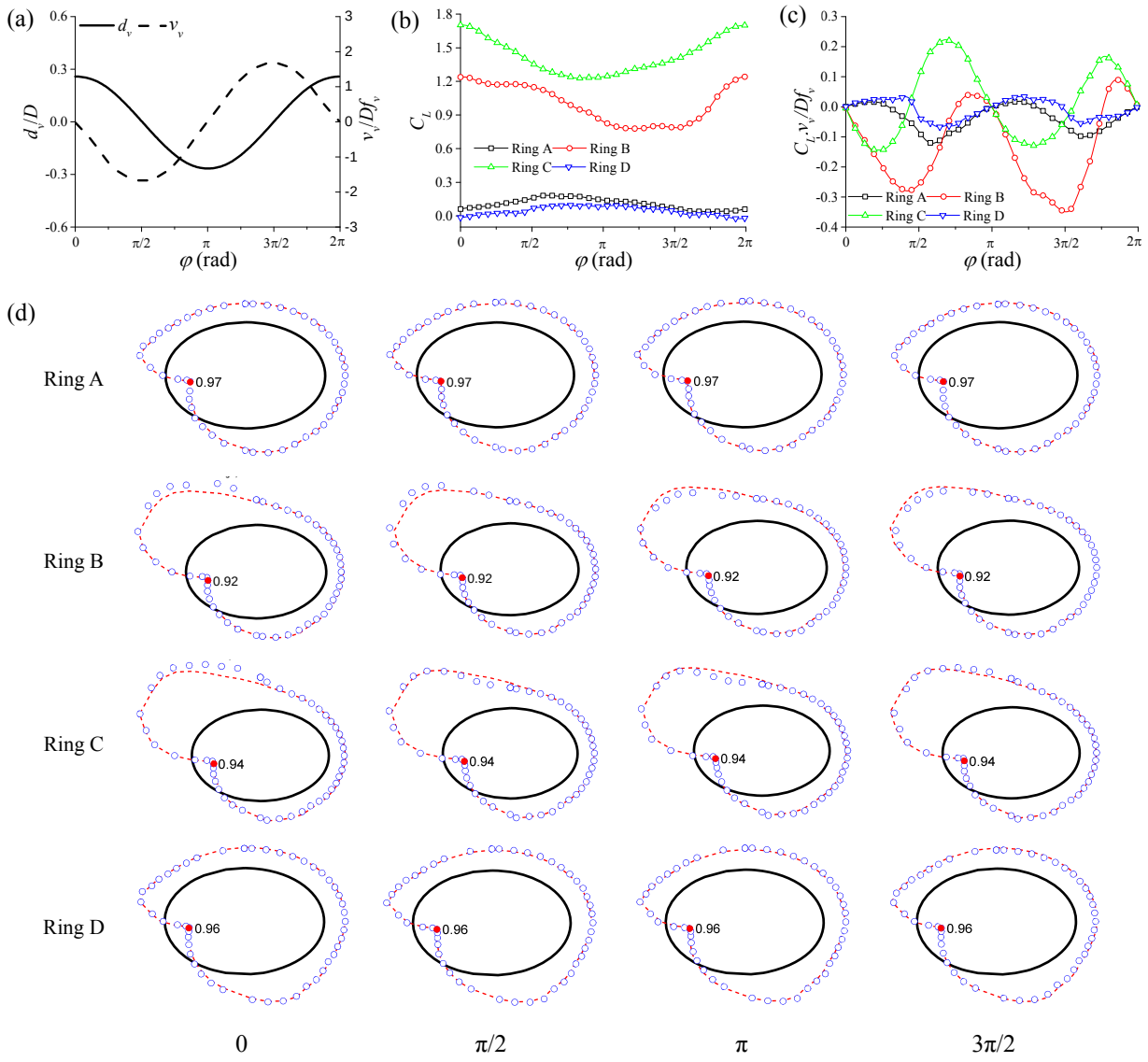

Fig. 8. Phase averaged results of (a) the normalized vertical displacement and velocity, (b) lift coefficients, (c) power input, and (d) pressure coefficient distributions.

Fig. 8 (b) and (d) show that the mean aerodynamic forces and pressures on Rings A and D are similar, as are those on Rings B and C. The flows around Rings A and D are in subcritical states, with no flow reattachment, while a clear separation bubble forms on Rings B and C, which are in the critical flow regime. The cylinder motion strongly interacts with the pressure coefficient distribution in the region of the separation bubble. The pressures in this region change periodically, as shown in Fig. 8 (d). This reveals that the aerodynamic forces in the critical Reynolds number range form stronger interactions with the motion than those in the subcritical range, because of the sensitivity of the wind pressure in the separation bubble region. The change of the pressure coefficients with the vibration phases are also shown in the form of the interaction in which the strong negative pressure area expands and contracts periodically, on average. The change comes with a variation of the final separation point, after which the wind pressure coefficient becomes uniform. This implies that the vibration is related to the reattachment and separation, which is not stable. Whereas the phase averaged lift coefficients on Rings A and D are similar, the lift coefficients on Rings B and C differ from each other in both value and variations with phase (Fig. 8 (b)). This difference causes them to have opposite contributions to the energy input. Fig. 8 (c) shows that the lift on Ring C, on average, makes a positive contribution to the vibrations through its input energy, while the lift on Ring B, on average, extracts energy, tending to reduce the

vibrations. This implies that the vibrations are excited by aerodynamic forces on many cross-sections, such as Ring C and are suppressed by many others, such as those on Ring B. The net result of these counteracting effects depends on the organization of the aerodynamic forces along the length. Fig. 8 (c) also shows the process of energy exchange with phase. Nikitas and Macdonald's results for a circular cylinder showed similar characteristics of the aerodynamic forces on different rings, with both energy input and absorption. One ring in their test was very effective in supporting the vibrations, with a phase delay that gave a positive power input for most phases. In the current case, the lift on Ring C input energy occurs only in two ranges of phase, $\varphi \approx \pi/2 - \pi$ and $3\pi/2 - 2\pi$.

5. Spanwise aerodynamic characteristics

5.1 Interactions along the length

To identify the lengthwise point along the cylinder where the aerodynamic forces have strong interactions with motion, the mean and standard deviations of the pressure coefficients on the four lines L1, L2, L3 and L4 (Fig. 1 (b)) are shown in Fig. 9. In the figure, $C_{P\sigma 1}$ means the standard deviation of the pressure coefficient, filtered through a narrow range of frequency, from 1.9 Hz to 2.1 Hz, and reflects the interaction strength. L_i/L is the normalized pressure tap position. The locations of the four tested rings are also indicated in Fig. 9. The pressures on L1 and part of L4, which are on the side of the cylinder with the separation bubble, show strong variations with the vibrations. The pressures on L2 and L3 show only small changes with vibration. Considering that the pressures on L4 and L2 comprise most of the lift coefficient, the vibrations are mainly influenced by the aerodynamic forces in the middle of the cylinder, from $L_i/L \approx 0.35$ to 0.65. The wind pressure distribution around the circumference in this range is similar to the distributions on Ring B and C shown in Fig. 6 (b). The reattachment can produce strong negative wind pressures on both L1 and L4, which are in the regions that have greater pressure variations and more negative mean pressure coefficients. Hence, the results imply that the vibrations depend on the local aerodynamic forces that are related to the reattachment. In the middle of the cylinder ($L_i/L \approx 0.2$-0.8), unlike the significant variations of pressure with location seen on L1 and L4, the pressures on L2 and L3, which are on the windward and leeward sides of the cylinder, are uniform. The results shown in Fig. 9 also reveal that the aerodynamic forces near both ends of the cylinder are unlikely to make significant contributions to the vibrations because of their relatively small standard deviations on all four lines.

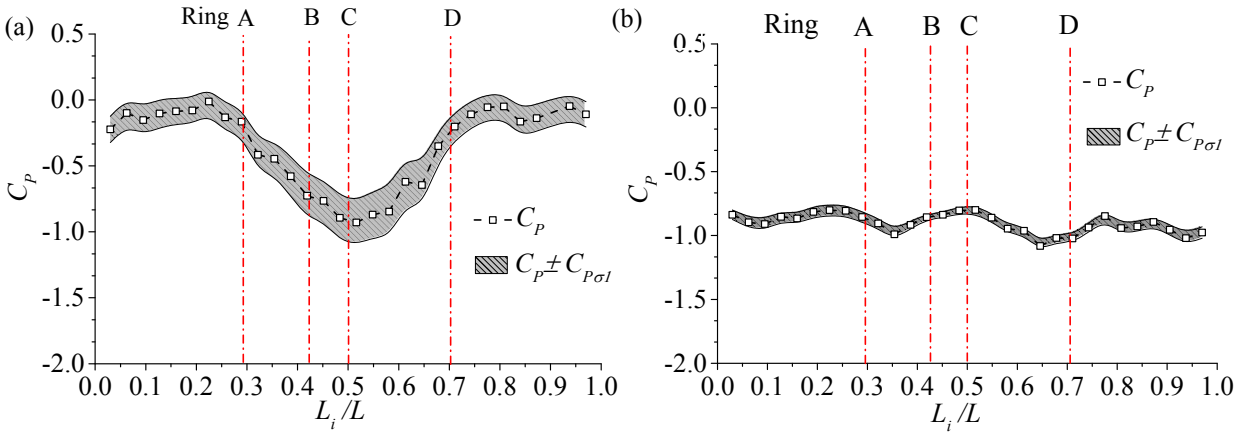

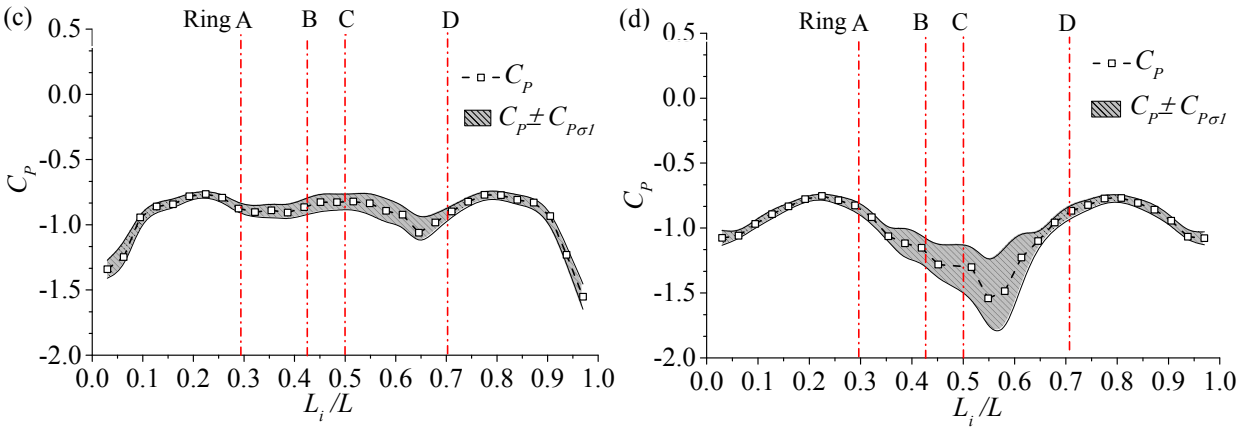

Fig. 9. Means and standard deviations of the pressure coefficients at α=26.98° and Re=1.75×10^5 on four tested lines: (a) L1, (b) L2, (c) L3 and (d) L4.

5.2 Typical mean pressure distribution states

In the static tests, the mean wind pressure coefficient distribution over the cross section can be characterized as one of three types, as shown in Fig. 10 (a), (b) and (c), which are termed States I, II and III for convenience. State I is a subcritical state in which the flow does not reattach on the cylinder surface, and a separation bubble is not formed. The flow around the cylinder exhibits regular vortex shedding with the Strouhal number 0.18, and the energy in the power spectrum is mainly concentrated in a narrow range around the vortex shedding frequency, e.g., 9.88 Hz at Re=1.24×10^5 and α=26°. With increasing Reynolds numbers, the flow starts to reattach on the rear of the cylinder, while the regular vortex shedding disappears, and the energy is distributed over a wide frequency range (Fig. 10 (b)). A separation bubble is then evident, and this new state is defined as State II. By further increasing the Reynolds number, the final separation point, which is downstream of the reattachment point, moves forward and forms the pressure coefficient distribution of State III, as shown in Fig. 10 (c). In this state, the energy still has a wide frequency distribution, and no regular vortex shedding is observed in the power spectrum of the lift coefficient. It should be noted that a transition condition between States I and II was observed in a few tests in which the force coefficients underwent jumps because the flow changes between non-reattached and reattached states. These jumps have been reported in studies of circular cylinders at critical Reynolds numbers at transitions from the subcritical regimes to single bubble regimes (Benidir et al., 2015; Nikitas and Macdonald, 2015). Similar to the static tests, the mean pressure coefficient distributions on the cylinder in the dynamic tests also show States I, II and III. Considering the data from all 164 dynamic tests, including the 18 with steady large amplitude vibrations, only State II exhibited strong interactions between the aerodynamic forces and motion. The example shown in Fig. 3, at α_0 =25.5° illustrates the whole process, from start to finish, of the large vibrations with increasing Reynolds number. There are no clear vibrations when the four rings are in State I (Re≤1×10^5). The cylinder starts vibrating when the aerodynamic forces on Rings B and C enter State II (Re>1.5×10^5), and then the vibrations stop when Ring C shows the characteristics of State III (Re>1.8×10^5).

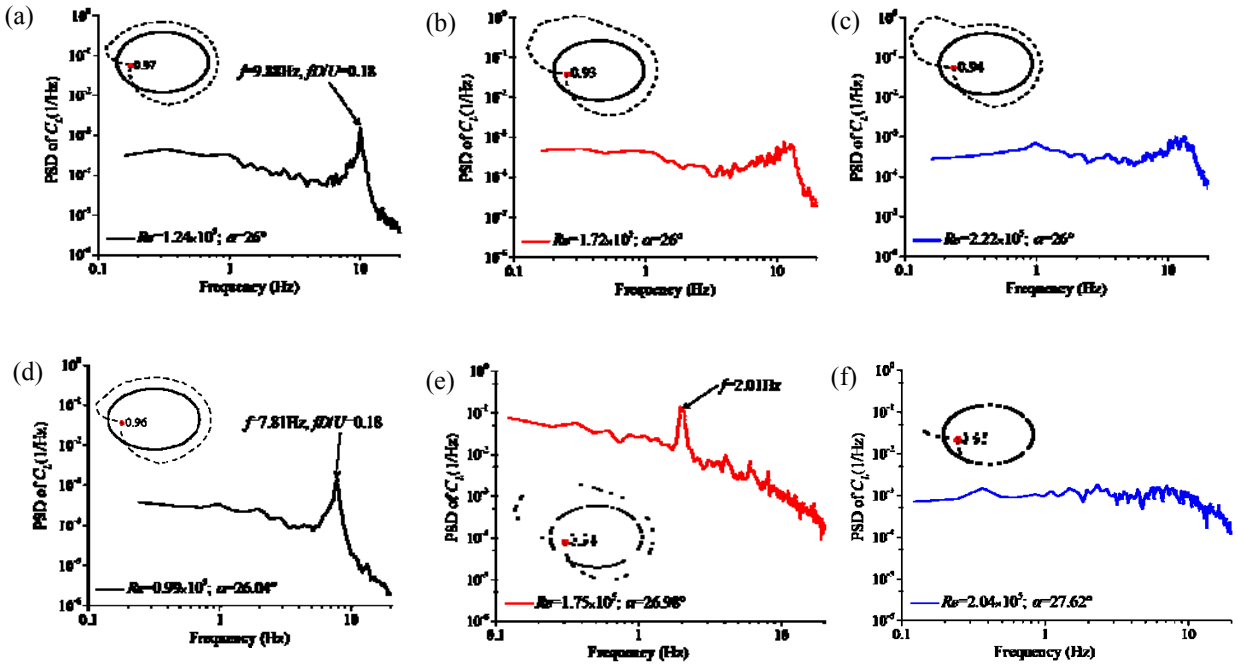

Fig. 10 Mean pressure coefficient distribution and power spectrum of the lift coefficient on Ring C for: (a) State I, static test, Re=1.26×10^5 and α=26°; (b) State II, static test, Re=1.72×10^5 and α=26°; (c) State III, static test, Re=2.22×10^5 and α=26°; (d) State I, dynamic test, Re=0.99×10^5 and α=26.05°; (e) State II, dynamic test, Re=1.75×10^5 and α=26.98° and (f) State III, dynamic test, Re=2.04×10^5 and α=27.62°.

5.3 Vibrations and spanwise flow state

By using the wind pressures on the four tested lines, the mean pressure distribution states can be estimated as a function of position along the cylinder. When the flow reattaches at the rear of the cylinder, as in State II, it produces more negative mean wind pressures on both lines L1 and L4. Once the final separation point moves forward, as in State III, the negative pressure on line L4 becomes weaker, and the pressure on line L1 does not obviously change. Fig. 11 (a) shows the variations of the normalized amplitudes with Reynolds numbers for an initial angle of attack α_0 =25.5°. Five cases at different Reynolds numbers are selected based on their vibration states. The cylinder does not vibrate in Case 1, starts unsteady vibrations in Case 2, reaches large steady amplitude vibrations in Case 3, stops vibrating in Case 4 and remains almost stationary in Case 5. Fig. 11 (b)-(f) show the mean pressure distributions on lines L1 and L4 for each case. Note that in addition to the Reynolds number increasing in each case, the mean angle of attack also changes slightly. In Case 1 Re=0.99×10^5, α=26.04°, no vibration occurs and the pressures indicate that the flow is in State I along the cylinder. In Case 2, Re=1.56×10^5, α=26.85°, and the mean pressures on L4 and L1 in a small section of the length in the middle of cylinder become lower, which means that the wind pressure distribution on the circumference in this region is in State II, and the flow reattaches at the rear of cylinder, while unsteady amplitude vibrations occur. With a small increase in the Reynolds number, in Case 3, where Re=1.68×10^5 and α=26.90°, State II exists over a longer length of the cylinder and large steady vibrations occur. In Case 4, where Re=1.80×10^5 and α=27.19°, the mean wind pressure on L4 becomes weaker in the middle of the cylinder, which indicates the wind pressure distribution is in State III, and the vibrations are reduced to small unsteady amplitudes. In Case 5, where Re=1.98×10^5 and α=27.52°, State III increases and the vibration amplitudes are unsteady and very small. Note that the middle of the cylinder undergoes the transition from State II to State III earlier than the rest of the cylinder. This may be related to the fact that the centre of the wind tunnel has a slightly higher wind speed and lower turbulence intensity than the areas close to the ends of the cylinder

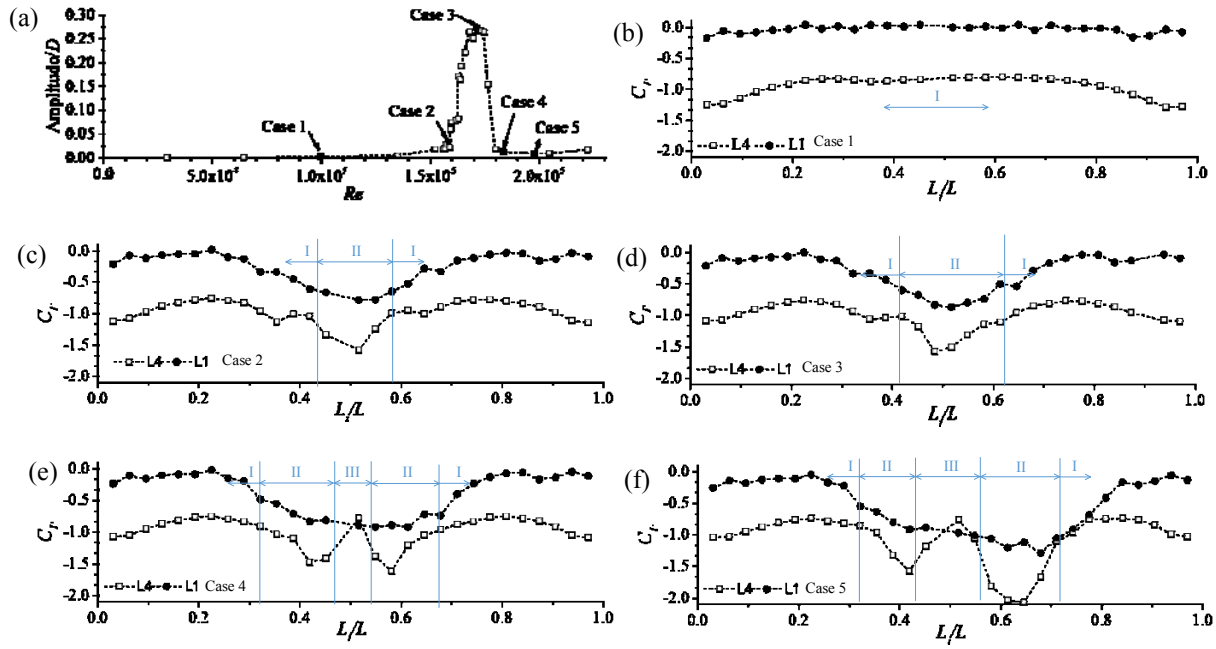

Fig. 11 (a) Normalized vibration amplitudes against Reynolds numbers for α_0=25.5°; (b)-(f) mean pressure coefficient distributions on L1 and L4 at: (b) Re=0.99×10^5, α=26.04°; (c) Re=1.56×10^5, α=26.85°; (d) Re=1.68×10^5, α=26.90°, (e) Re=1.80×10^5, α=27.19° and (f) Re=1.98×10^5, α=27.52°.

Matsumoto and Yagi explain the excitation of dry galloping in terms of the level of vortex mitigation (Matsumoto et al., 2010). The results of this study are consistent with this explanation in so far as all vibrations observed showed no clear vortex shedding at the four tested rings, but they do not explain the cessations of the vibrations when there is still no vortex shedding. Matteoni and Georgakis suggested that their observations of both stable responses and divergent vibrations of circular cylinders at critical Reynolds numbers indicate the sensitivities of the behaviours to microscopic geometrical imperfections of the cable model. In the present case, the imperfections at least of the geometric shape, if not those of the surface roughness, may be ignored in comparison with the lack of roundness of the elliptical cross-section itself. Nikitas and Macdonald reported a pressure distribution on one side of a circular cylinder which is similar to those of our results in State II, and they suggested dry galloping may be related to unsteady flow transitions (Nikitas and Macdonald, 2015). Unlike previous studies, the current study of an elliptical cylinder found that the vibrations are observed only when the flow starts reattaching on the rear. By combining the explanation mentioned above and our observations, the vibrations can be understood in two aspects. At first, the vortex shedding ceased when the flow starts reattaching to the cylinder, making the wide band energy distribution occur at a lower frequency that is close to the natural frequency. In contrast, the reattachment starts at the rear, which is not stable since the reattachment point is easily influenced by disturbances such as small motions, and this unstable reattachment is more likely to interact with any motion. Once the reattachment and final separation points move forward, they become more stable, and the stable flow may stop the vibrations, even though there is still no vortex shedding. Another factor influencing the vibrations is the distribution of the loading along the length. Because the aerodynamic forces can either input or extract energy during the vibrations, the amplitudes of the responses are determined by the organizations of the aerodynamic forces along the length of the cylinder, which may include all three states at different points along the cylinder. This behaviour may also make it less likely for such vibrations to occur on a long cylinder in non-uniform flows.

6. Conclusions

In conclusion, based on the observed large vibrations and pressure distributions on an elliptical cylinder in the critical Reynolds number range, the vibrations shown in this study cannot be explained by quasi-steady theory, even though the reduced velocity is from 35 to 40. The characteristics of the vibrations are strongly related to the sensitivities of the flow at the early reattachment stage in the critical Reynolds number range and the organization of the aerodynamic forces along the length of the cylinder.

The strong interactions and vibrations are observed only when the flow reattaches at the rear of the cylinder in the early stage of the critical Reynolds number transition, and are mainly attributed to the pressure fluctuations in the region of the separation bubble. Therefore, the reattachment may induce vibrations only if it is not stable enough when it occurs at the rear of the cylinder. Because the interactions can either input or absorb energy from the vibrations, an ideal organization of the forces along the cylinder is also needed for a net excitation. Once the reattachment point moves forward, and the separation bubble becomes stable with increasing Reynolds number, no further vibrations are observed.

Acknowledgements

The authors gratefully acknowledge the support of the National Natural Science Foundation of China (Grant No. 51378323), Natural Science Foundation of Hebei Province (Grant No. E2017210107), Collaborative Innovation Centre of Preventing Disasters and Reducing Damages for Large Infrastructures in Hebei Province and the China Scholarship Council for Wenyong Ma's visit at University of Bristol.

References

Alonso, G., Meseguer, J., Sanz-Andrés, A., Valero, E., 2010. On the galloping instability of two-dimensional bodies having elliptical cross-sections. Journal of Wind Engineering and Industrial Aerodynamics 98, 438-448.

Benidir, A., Flamand, O., Gaillet, L., Dimitriadis, G., 2015. Impact of roughness and circularity-defect on bridge cables stability. Journal of Wind Engineering and Industrial Aerodynamics 137, 1-13.

Flamand, O., Boujard, O., 2009. A comparison between dry cylinder and rain-wind induced excitation, in: Proceedings of the 5th European and African Congress on Wind Engineering, 19-23.

Fung, Y.C., 1955. An Introduction to the Theory of Aeroelasticity. Wiley, New York.

Hoxey, R.P., Reynolds, A.M., Richardson, G.M., Robertson, A.P., Short, J.L., 1998. Observations of Reynolds number sensitivity in the separated flow region on a bluff body. Journal of Wind Engineering and Industrial Aerodynamics 73, 231-249.

Jakobsen, J.B., Andersen, T.L., Macdonald, J.H.G., Nikitas, N., Larose, G.L., Savage, M.G., McAuliffe, B.R., 2012. Wind-induced response and excitation characteristics of an inclined cable model in the critical Reynolds number range. Journal of Wind Engineering and Industrial Aerodynamics 110, 100-112.

Ma, W., Macdonald, J.H.G., Liu, Q., Nguyen, C.H., Liu, X., 2017. Galloping of an elliptical cylinder at critical Reynolds number and its quasi-steady prediction. Journal of wind engineering and industrial aerodynamic 168, 110-122.

Ma, W.Y., Liu, Q.K., Du, X.Q., Wei, Y.Y., 2015. Effect of the Reynolds number on the aerodynamic forces and galloping instability of a cylinder with semi-elliptical cross sections. Journal of wind engineering and industrial aerodynamic 146, 71-80.

Matsumoto, M., Yagi, T., Hatsuda, H., Shima, T., Tanaka, M., Naito, H., 2010. Dry galloping characteristics and its mechanism of inclined/yawed cables. Journal of Wind Engineering and Industrial Aerodynamics 98, 317-327.

Matteoni, G., Georgakis, C.T., 2012. Effects of bridge cable surface roughness and cross-sectional distortion on aerodynamic

force coefficients. Journal of Wind Engineering and Industrial Aerodynamics 104–106, 176-187.
Matteoni, G., Georgakis, C.T., 2015. Effects of surface roughness and cross-sectional distortion on the wind-induced response of bridge cables in dry conditions. Journal of Wind Engineering and Industrial Aerodynamics 136, 89-100.
Nikitas, N., Macdonald, J.H.G., 2015. Aerodynamic Forcing Characteristics of Dry Cable Galloping at Critical Reynolds Number. European Journal of Mechanics - B/Fluids 49, 243-249.
Nikitas, N., Macdonald, J.H.G., Jakobsen, J.B., Andersen, T.L., 2012. Critical Reynolds number and galloping instabilities: experiments on circular cylinders. Exp Fluids 52, 1295-1306.
R.D.Blevins, 2001. Flow-induced Vibration, Second ed. Van Nostrand Reinhold, New York.
Schewe, G., 1986. Sensitivity of transition phenomena to small perturbations in flow round a circular cylinder. J Fluid Mech 172, 33-46.
Zdravkovich, M.M., 1997. Flow Around Circular Cylinders Vol 1: Fundamentals. Oxford University Press, New York.